Journal of Materials Chemistry A

ROYAL SOCIETY OF CHEMISTRY

PAPER

View Article Online
View Journal | View Issue



Cite this: J. Mater. Chem. A, 2024, 12, 30821

# Controlling $CO_2$ flux in a $CO_2$-permeable membrane with a $H_2O$ driving force†

Jacqueline A. Penn, Wenting Hu, Ian S. Metcalfe and Greg A. Mutch *

Gas separation membranes hold significant promise for carbon capture and storage (CCS) as they offer high modularity in combination with technical simplicity. It is routinely expected that a difference in the partial pressure of $CO_2$ (*i.e.*, a $CO_2$ driving force) across a $CO_2$-permeable membrane dictates $CO_2$ flux. Here, however, we show that in a molten-salt membrane fabricated using molten hydroxides, a $H_2O$ driving force in the opposite direction to $CO_2$ permeation exerts control. We demonstrate this by using the opposing $H_2O$ driving force to operate the membrane in ways that challenge the conventional understanding of $CO_2$-permeable membranes. For example, increasing the $CO_2$ flux whilst decreasing the $CO_2$ driving force. Throughout, we employ a model membrane support to facilitate recovery (and subsequent characterisation) of the molten salt, showing that membranes fabricated using molten hydroxides transform into majority molten carbonate membranes during $CO_2$ separation. The carbonate : hydroxide ratio is shown to be a function of time, temperature, and gas-phase composition, and high carbonate : hydroxide ratios are correlated with high $CO_2$ fluxes. Overall, our work demonstrates that molten-salt membranes evolve, and that a $H_2O$ driving force can be used to control $CO_2$ flux.

Received 19th July 2024
Accepted 5th October 2024

DOI: 10.1039/d4ta05021e

rsc.li/materials-a



## 1. Introduction

To limit global warming to less than 1.5 °C above pre-industrial levels by 2100, global $CO_2$ emissions must reach net-zero by 2050. Carbon capture and storage (CCS) is expected to play a critical role in enabling the transition to net-zero.[1] CCS is an attractive option as it can often be deployed without significant process changes, and because it is currently a lower-cost option than many electrification approaches for emission-intensive industries (*e.g.*, cement, iron, steel, refineries, chemicals *etc.*).[2] In addition, it can offer the potential for negative emissions in certain configurations, *i.e.*, in direct air capture,[3] and bioenergy with CCS processes.[4]

There are clear opportunities for membranes in CCS processes, particularly in situations where there are high concentrations of $CO_2$ in the feed gas (*e.g.*, cement, iron, steel, refineries, chemicals *etc.*), where lower capture rates are tolerable, and at smaller scales. For example, with a feed gas containing 10% $CO_2$, the energy requirement for a two-stage polymeric membrane process with a capture rate of 60% and >99% $CO_2$ product is the same as an amine-based solvent process with a capture rate of 90% and >99% $CO_2$ product. However, if the feed gas contains 30% $CO_2$, the membrane process requires less than half the energy of the solvent process.[5] Similarly, a comparative techno-economic analysis of post-combustion $CO_2$ capture (12% $CO_2$ feed gas; 96% $CO_2$ product) using a modern amine solvent, solid adsorbent, and a polymeric membrane found that the adsorbent and membrane processes are more cost-competitive with the solvent process when low capture rates are tolerable and at small scales (<100 t $CO_2$ per day).[6]

Whilst various polymeric membrane materials and process configurations have been investigated for carbon capture, few have made it beyond pilot-plant scale (TRL 5–6).[1,7] Inorganic membranes have been investigated for carbon capture even less, due largely to disadvantages (relative to polymeric membranes) in terms of processability, brittleness, and cost. Nonetheless, at the lab scale (TRL 3–4), they appear to offer good chemical and thermal stability, and in certain configurations, very high $CO_2$ perm-selectivity (a key performance metric for application in CCS). For example, supported molten-salt membranes (porous inorganic support, infiltrated with a molten salt), have been shown to provide exceptionally high $CO_2$ perm-selectivity when they are fabricated using molten carbonates ($CO_2$ permeability of $10^{-12}$ to $10^{-10}$ mol $m^{-1}$ $s^{-1}$ $Pa^{-1}$ and $CO_2/N_2$ selectivity up to 1000).[8] For comparison, state-of-the-art polymeric membranes (TRL 3–4) offer $CO_2$ permeability one order of magnitude lower ($10^{-13}$ mol $m^{-1}$ $s^{-1}$ $Pa^{-1}$) and $CO_2/N_2$ selectivity several orders of magnitude lower (10),[9] whilst for post-combustion CCS in general, $CO_2$ permeability on the order of $10^{-13}$–$10^{-12}$ mol $m^{-1}$ $s^{-1}$ $Pa^{-1}$ in combination with

*Materials, Concepts & Reaction Engineering (MatCoRE) Group, School of Engineering, Newcastle University, Newcastle upon Tyne, NE1 7RU, UK. E-mail: greg.mutch@newcastle.ac.uk*

† Electronic supplementary information (ESI) available. See DOI: https://doi.org/10.1039/d4ta05021e

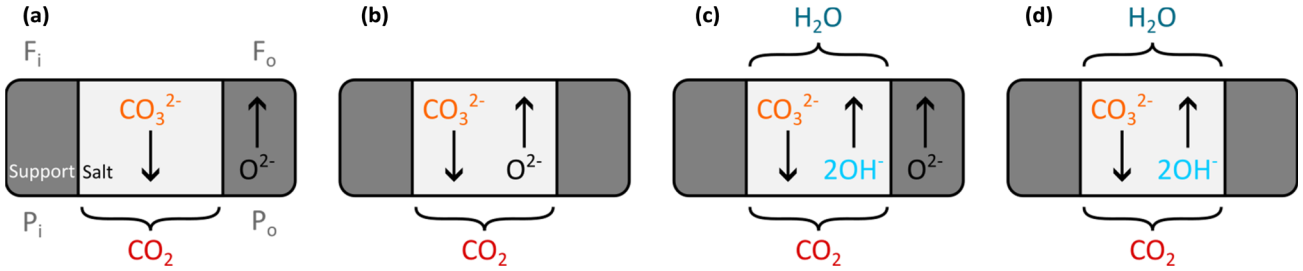


Fig. 1 Proposed mechanisms of counter-diffusion of ionic species in supported molten-salt membranes. (a) Molten carbonate salt with an oxide-ion conducting support and (b) an inert support. (c) Molten carbonates in the presence of a $H_2O$-containing sweep gas, or molten hydroxides, with an oxide-ion conducting support and (d) an inert support. In (a)–(d), a $CO_2$-containing feed gas is supplied to the top surface of the membrane, and in (c) and (d), a $H_2O$-containing sweep gas is supplied to the bottom surface of the membrane. Permeation of $CO_2$ would therefore occur from top to bottom, and $H_2O$ from bottom to top, as shown here with curved brackets. In (a), $F_i$ and $F_o$ indicate the $CO_2$ feed-side chamber inlet and outlet respectively, and $P_i$ and $P_o$ indicate the $CO_2$ permeate-side chamber inlet and outlet respectively. The sweep gas is introduced at $P_i$. Note that this labelling, as well as "Support" and "Salt", is applicable for (a)–(d).

$CO_2/N_2$ selectivity of 50–100 is required.[10] Thus, supported molten-salt membranes appear to offer sector-leading $CO_2$ perm-selectivity, at or beyond the level required for application.

The wide range of observed $CO_2$ perm-selectivity in supported molten-salt membranes is due, at least in part, to the use of a very wide array of solid support materials and membrane geometries. Support materials have included nominally inert ceramics (*e.g.*, $Al_2O_3$),[11–13] oxide-ion conducting ceramics (*e.g.*, doped $CeO_2$),[11,14] mixed electron and oxide-ion conducting ceramics (*e.g.*, $La_{0.6}Sr_{0.4}Co_{0.8}Fe_{0.2}O_{3-\delta}$),[15,16] and metals (*e.g.*, Ag).[17–19] Support geometries have included pellets,[11,12,14–19] hollow fibres,[13,20] and tubes.[19,21–23] As pore volume and tortuosity is expected to impact $CO_2$ flux,[24–26] these are introduced and/or controlled using a variety of methods, most often by partial sintering of ceramic powders,[11,12,14–17,19] but also by electrochemical dealloying,[18] phase inversion,[13] and tape-casting and freeze-drying.[27] To produce pores with very low tortuosity, advanced manufacturing techniques have also been employed, including laser drilling,[19,23] and laser-directed solidification.[28]

Such a wide array of chemical and physical properties can make detailed comparisons of membrane performance and permeation mechanism difficult, particularly in the absence of thorough characterisation, which is often the case. Nonetheless, various permeation mechanisms relying on the counter-diffusion of ionic species have been proposed to explain experimental observations (Fig. 1). For example, in the case of oxide-ion conducting supports, the counter-diffusion of oxide ions in the solid support, and carbonate ions in the molten carbonates is proposed (Fig. 1a).[29] Due to the lower ionic conductivity of solid supports compared to molten carbonates, increasing the solid fraction of the membrane can lead to higher $CO_2$ fluxes.[29]‡ In the case of inert solid supports, as there is no route for the transport of ionic species in the solid, $CO_2$ permeation is expected to be facilitated by the molten carbonate alone. Low $CO_2$ fluxes observed for membranes with inert supports have been justified based on the low concentration of oxide ions in molten carbonates, compared to the majority ions (*i.e.*, alkali metals and carbonate) (Fig. 1b).

The composition of molten carbonates has also been discussed in the context of $H_2O$-containing sweep gases. For example, in $CeO_2$,[14] $BaZr_{0.8}Y_{0.2}O_{3-\delta}$,[30] and $Sc_{0.1}Ce_{0.01}Zr_{0.89}O_{1.95}$,[31] supported molten-salt membranes, $CO_2$ flux increases of 30 to 300% were observed for $H_2O$-containing sweep gases, compared to 'dry' sweep gases.§ It was suggested that hydroxide ions in the molten carbonate, formed *via* reaction with $H_2O$, contributed to an increased flux. In only one study to date, the molten carbonates normally used during membrane fabrication were substituted with molten hydroxides (we note here that this membrane was tested with a $H_2O$-containing sweep gas also, and employed a $CeO_2$ support).[32] With $H_2O$-containing sweep gases, it is proposed that counter-diffusion of hydroxide and carbonate ions occurs in the molten salt, in addition to the counter-diffusion of oxide ions in the solid support and carbonate ions in the molten salt (Fig. 1c), leading to high $CO_2$ flux.

In the case of the molten-salt membrane fabricated using molten hydroxides, the authors made the interesting suggestion that the molten-salt composition changes in response to the partial pressure of $CO_2$ in the feed gas. For example, a surprising increase in $CO_2$ permeability observed with a decrease in the feed-gas $CO_2$ partial pressure was attributed to the lower $CO_2$ partial pressure leading to the molten salt having a lower carbonate : hydroxide ratio (and therefore a higher overall ionic conductivity, as molten hydroxides have a higher ionic conductivity than molten carbonates).[32] This suggestion that the composition of molten salts may change in response to gas phase conditions is particularly interesting as it suggests that the starting composition of a molten-salt membrane may be relatively unimportant. A deeper understanding of membrane performance therefore requires detailed characterisation of the molten salt as a function of operating conditions.

‡ Assuming due consideration is given to percolation of the molten salt at the highest solid support fractions and noting that the condition of maximum ambipolar diffusion will be different at different temperatures, and for different support materials.

§ Apostrophes around dry (*i.e.*, 'dry') denotes that the precise $H_2O$ concentration in the sweep gases were not measured/provided.

A final complication for all the work on supported molten-salt membranes is in understanding the exact nature of the $CO_2$ flux-driving force relationship. Recent work studied the partial pressure dependence of $CO_2$ flux in a membrane with an oxide-ion conducting support and molten carbonates under 'dry' conditions (Fig. 1a).§ This was achieved by varying the porosity of the support and therefore solid fraction of the membrane.[26] Whilst the authors noted that $CO_2$ flux generally increased with $CO_2$ partial pressure in the feed gas, there were important differences noted. When $CO_2$ flux was controlled by carbonate-ion conduction in the molten salt (low porosity support/high solid fraction), $CO_2$ flux showed a logarithmic dependence on $CO_2$ partial pressure (eqn (1)). When $CO_2$ flux was controlled by oxide-ion conduction in the solid phase (high porosity support/low solid fraction), a power-law dependence on $CO_2$ partial pressure was shown (eqn (2)),

$$J_{CO_2} \propto \ln\left(\frac{p'_{CO_2}}{p''_{CO_2}}\right) \quad (1)$$

$$J_{CO_2} \propto \left(p'^{n}_{CO_2} - p''^{n}_{CO_2}\right) \quad (2)$$

where $J_{CO_2}$ is the flux of $CO_2$, and $p'_{CO_2}$ and $p''_{CO_2}$ are the partial pressures of $CO_2$ at the feed and permeate sides of the membrane, respectively. Thus, one might expect $CO_2$ flux in molten-salt membranes fabricated using molten carbonates and inert supports to follow a logarithmic relationship (as there is no route for transport in the solid support, and therefore carbonate-ion conduction must control flux). Indeed, this relationship was observed in our recent work under dry sweep-gas conditions (<100 ppm $H_2O$).[33] However, with $H_2O$ present in the sweep gas, the $CO_2$ driving force no longer had a strong effect on $CO_2$ flux, and instead, a $H_2O$ driving force appeared to exert control (eqn (3)),

$$J_{CO_2} \propto \ln\left(\frac{p''_{H_2O}}{p'_{H_2O}}\right) \quad (3)$$

where $J_{CO_2}$ is the flux of $CO_2$, and $p'_{H_2O}$ and $p''_{H_2O}$ are the partial pressures of $H_2O$ at the feed and permeate sides of the membrane, respectively. Note that as $H_2O$ was fed to the permeate side of the membrane (in the sweep gas), the driving force for $H_2O$ (and therefore, $H_2O$ permeation) was in the opposite direction to the $CO_2$ driving force (and therefore, $CO_2$ permeation). In the same work we showed that carbonate-like ions in molten carbonates can act as a carrier for both $CO_2$ and $H_2O$, with their transport occurring in opposite directions.[33] The mechanism involved several energetically-viable transport routes, with complex, inter-connected equilibria and different carrier forms, so the reader is referred to that work for further detail. Overall, however, $H_2O$ at the $CO_2$ permeate-side, gas-membrane interface drove the release of $CO_2$ from that interface and $CO_2$ at the $CO_2$ feed-side, gas-membrane interface drove the release of $H_2O$ at that interface, from a shared carbonate-like carrier.

Based on our recent work and the discussion above, we were motivated to investigate the potential for changes to molten-salt composition with operating conditions *e.g.*, time, temperature, and gas-phase composition, and to understand the role of the $H_2O$ driving force on $CO_2$ flux in membranes fabricated using molten hydroxides. To limit permeation to the molten salt alone, and to attempt to simplify mechanism (Fig. 1d), we prepared a model, inert support with pores of very low tortuosity (laser-drilled alumina) (Fig. 2), which was infiltrated with molten hydroxides. A series of permeation experiments and corresponding characterisations of recovered molten salts were performed to understand the role of $H_2O$ in $H_2O$-containing feed and sweep gases on $CO_2$ flux, and on molten-salt composition. Importantly, we monitored the $H_2O$ concentration at both sides of the membrane continuously (whilst also monitoring the permeate-side outlet for $CO_2$). This is unusual, as it has been common practice to only measure the permeate-side outlet (to measure $CO_2$ flux) in experiments with supported molten-salt membranes. This allowed us to experimentally demonstrate the counter-permeation of $CO_2$ and $H_2O$ in a membrane fabricated using molten hydroxides for the first time. Moreover, there was a very clear influence of both the

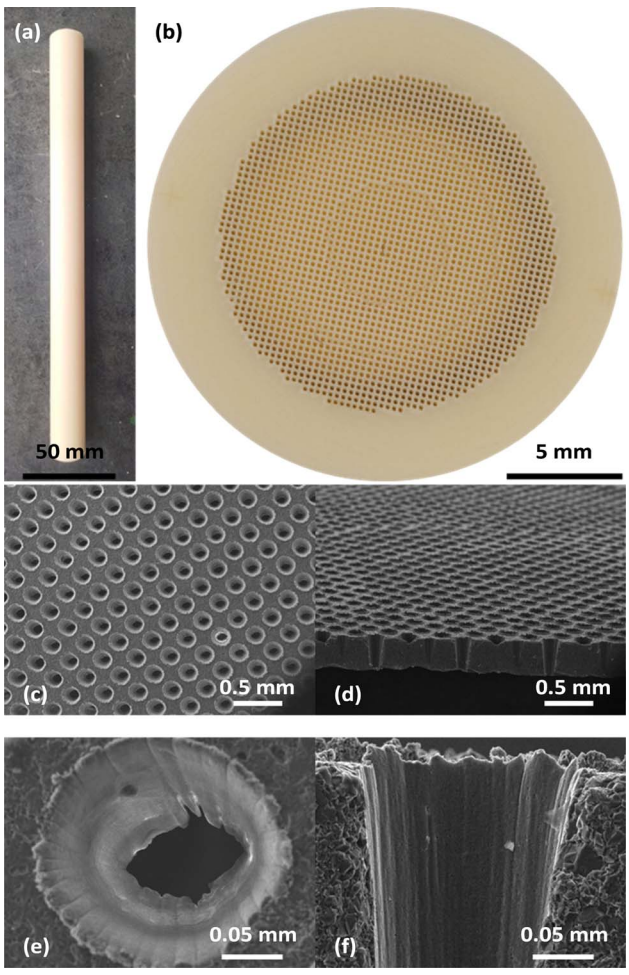


Fig. 2 Molten-salt membrane support. (a) Dense alumina tube with one closed end. (b) Laser-drilled holes on the closed end, and (c–f) SEM images of the laser-drilled holes in top-down and cross-section views.

molten-salt composition (carbonate : hydroxide ratio) and particularly the $H_2O$ driving force (from $CO_2$ permeate side to $CO_2$ feed side) on $CO_2$ flux (from $CO_2$ feed side to $CO_2$ permeate side).

## 2. Experimental

### 2.1 Materials

Lithium hydroxide (powder, reagent grade, ≥98%), sodium hydroxide (powder, reagent grade, 97%), potassium hydroxide (powder, for synthesis), hydrochloric acid solution (0.1 mol $l^{-1}$ reagent grade) and phenolphthalein solution (0.5% w/w in ethanol : water (1 : 1)) were purchased from Sigma-Aldrich. Lithium carbonate (powder, 99%), sodium carbonate (powder, 98%) and potassium carbonate (granular, ≥99%) were purchased from Alfa Aesar. Bromocresol green (sodium salt, 0.04% w/v aqueous solution) was purchased from Thermo Fisher Scientific. Fully dense alumina tubes with one closed end were purchased from Precision Ceramics (length 235 ± 1.6 mm, outer diameter (OD) 19.05 mm, inner diameter (ID) 17.78 mm, OD/ID ± 0.635 mm, and closed-end thickness 0.46 mm) (Fig. 2a). The closed ends of the tubes were laser drilled by Laser Micromachining Ltd to form an array of ~2000 truncated conical holes (~150 μm entrance, ~50 μm exit) on a square pitch of ~250 μm (Fig. 2b–f). A perfluoropolyether based, chemically inert, high-temperature vacuum grease (PFPE 501) was purchased from Apiezon. All gases were supplied by BOC.

### 2.2 Membrane preparation, membrane reactor and flow system

A mixture containing 43.5 mol% lithium hydroxide, 31.5 mol% sodium hydroxide, and 25 mol% potassium hydroxide was prepared, and thoroughly mixed in a Fluxana MUK mixer, inside a nitrogen glove box (to avoid deliquescence and limit reaction with atmospheric $CO_2$). The composition of the hydroxide mixture was chosen as upon full conversion to carbonate, the carbonate ternary eutectic would form. The hydroxide mixture was stored in the glove box, with portions weighed out and removed periodically to make pellets for permeation experiments. These pellets were prepared by pressing the amount of hydroxide mixture required to fill the volume of the laser-drilled holes (upon melting) at 3 tons in an Atlas Power T25 hydraulic press, with the pellets having the diameter required to cover the laser-drilled area.

The laser-drilled, closed-end alumina tube was housed in a custom-made membrane reactor,[19,23,33] with gas inlets/outlets and a thermocouple port positioned near the closed end of the alumina tube (Fig. S1a†). The tube (outer diameter ~19 mm) was placed inside the stainless-steel base of the membrane reactor (inner diameter ~20 mm), and vacuum grease was applied around this connection to form the seal. The pellet of hydroxide mixture was placed on the laser-drilled, closed end of the tube. A quartz cover was then sealed to the base of the membrane reactor using a rubber O-ring under compression. This arrangement creates two chambers: a $CO_2$ feed-side chamber inside the alumina tube, and a $CO_2$ permeate-side chamber between the alumina tube and quartz cover, with both chambers having a gas inlet and outlet (Fig. S1a†). Hereafter, these are frequently referred to simply as feed-side chamber and permeate-side chamber. Based upon the residence time distribution response for both chambers (Fig. S2†), the membrane was considered to be exposed to the outlet conditions of each chamber.

The constructed membrane reactor was located within a vertical split-tube furnace (Vecstar) and connected to an automated flow system containing mass flow controllers (Brooks) and 4-way electronic valves (VICI), which allowed for the delivery of feed- and sweep-gas streams (Fig. S1b and c†). All flow rates, for all experiments and gas mixtures, were set to 50 ml $min^{-1}$ (NTP), by measuring the appropriate gas-stream outlet using an electronic flow meter (GFM Pro, Thermo Scientific).

The flow system permitted the independent humidification of the feed- and sweep-gas streams, due to the presence of two in-line, water-filled permeation tubes. These consist of two water-filled reservoirs, separated from the gas streams by two water-permeable membranes, contained within two furnaces. The quantity of water transferred across the water-permeable membranes, and therefore the resulting $H_2O$ concentration in the gas streams, was controlled by varying the temperature of the furnaces (Fig. S3†).

### 2.3 Permeation experiments and measurement of $CO_2$ and $H_2O$ flux

To melt the hydroxide mixture, and infiltrate the laser-drilled holes, the membrane reactor was heated to the experimental temperature at 2 °C $min^{-1}$. During heating, ~1% $H_2O$ in Ar was supplied to both the feed-side and permeate-side chamber inlets, to limit decomposition of the hydroxide mixture.[34] At the experimental temperature, the feed-side chamber inlet was switched to a $CO_2$ in $N_2$ mixture, whilst the permeate-side chamber inlet remained as Ar (throughout the experimental campaign, the feed- and permeate-side gas streams were humidified to different extents). The presence of different inert gases in the feed- and permeate-side streams ($N_2$ and Ar) permitted the detection of transmembrane leaks. Experiments were stopped if $N_2$ was detected significantly above background levels in the permeate-side outlet, or if $N_2$ levels were seen to be increasing (see below).

The $CO_2$ and/or $H_2O$ mole fraction in the feed- and permeate-side outlet streams were monitored by two, in-line infrared analysers (LI-COR, LI-850 $CO_2/H_2O$). The mole fraction of $N_2$ in the permeate-side outlet stream was also monitored by a quadrupole mass spectrometer (Hiden, QGA), connected to the outlet of the corresponding infrared analyser. The infrared analysers and mass spectrometer were calibrated to account for systematic error, and any air ingress into the membrane reactor, flow system, or analytical equipment. This was performed by flowing Ar (99.999%, total impurities ≤10 ppm maximum, typical impurity concentrations: 3 ppm $H_2O$, 6 ppm $N_2$, 2 ppm $O_2$) through the flow system, membrane reactor, infrared analysers, and mass spectrometer to obtain a background. The

 

background measured before an experiment confirmed the absence of significant leaks into the experimental apparatus, whilst the background measured after an experiment was subtracted from the collected experimental data. Typically, the background levels were ~200 ppm of $N_2$ and ~10 ppm of $CO_2$. Gases of certificated mole fraction (369 ppm $CO_2$ in Ar, 400 ppm $N_2$ in Ar, and 903 ppm $H_2O$ in Ar) were used to calibrate the infrared analysers and mass spectrometer. Instrumental drift in the mass spectrometer was also accounted for by normalising $CO_2$, $H_2O$, and $N_2$ signals against Ar (majority species).

The mole fraction of $CO_2$ and/or $H_2O$ in the permeate-side outlet was converted to flux (mol $s^{-1}$ $m^{-2}$) using eqn (4),

$$J_i = \frac{y_i Q_G}{60 \times 22400} \times \frac{1}{A} \quad (4)$$

where $J_i$ is the flux of i (here, $CO_2$ or $H_2O$), $y_i$ is the mole fraction of i in the gas phase at the outlet, $Q_G$ is the volumetric flow rate at the outlet (ml $min^{-1}$), and $A$ is the permeate-side area of the membrane ($m^{-2}$). As two supports were used throughout the experimental campaign, the permeate-side areas used were 0.35 and 0.47 × $10^{-5}$ $m^{-2}$, based on the specific number of laser-drilled holes in each.

### 2.4 Membrane characterisation

Following permeation experiments, the molten salt component of the membrane was recovered by sonicating the laser-drilled, closed-end of the cooled membrane in ~60 ml of deionised water for 30 minutes at 35 °C. Subsequently, 8 ml samples were titrated against 0.1 mol $l^{-1}$ HCl, using the two indicators separately (phenolphthalein and bromocresol green). Phenolphthalein indicates ($v_1$) upon complete conversion of $CO_3^{2-}$ to $HCO_3^-$, and bromocresol green indicates ($v_2$) upon complete conversion of $CO_3^{2-}$ to $H_2CO_3$. The titration was performed in triplicate, with the mean volume of HCl consumed used in calculations; $(v_2 - v_1)$ for $CO_3^{2-}$, and $(2(v_1) - v_2)$ for $OH^-$.[32,35,36] The reliability of the titration was tested both for accuracy compared to known mixtures of hydroxides and carbonates, and for any effect that cooling procedures (rate and atmosphere) had on composition. We note here that the titration was shown to accurately identify the composition of seven different known mixtures, and that the largest difference between actual and measured composition was <4% (Table S1†). Moreover, the rate of cooling and cooling atmosphere did not appear to have a significant effect (Table S2†), and therefore all membranes were cooled in dry Ar (Ar with ≤3 ppm $H_2O$) at 5 °C $min^{-1}$.

Samples of the laser-drilled, closed-end alumina tubes, both prior to permeation experiments and following several, extended permeation experiments lasting a total of ~800 h (~500 h at 400–700 °C, and ~300 h of heating/cooling), were prepared by cutting with a diamond saw (Top Tech Precision, CL40). A first cut removed the closed end of the tubes, to create a pellet shape containing the laser-drilled holes. A second cut split the pellet shape in two, creating semi-circular pieces and revealing the cross section. The prepared samples were rinsed with deionised water, and sonicated in deionised water for 30 minutes at 35 °C. For SEM imaging and EDX analysis, the semi-circular samples were carbon coated (EMScope TB500) before analysis with a JSM-IT510 InTouchScope™ Scanning Electron Microscope with integrated EDX. Images and EDX spectra were taken under high vacuum with secondary electron detection using an accelerator voltage of 20 kV and a working distance of 10 mm. Images and EDX spectra were collected from various sample orientations to access different surfaces, and within the laser-drilled holes (*i.e.*, the cross-section view). Samples without carbon coating were analysed by Raman spectroscopy (Horiba LabRAM HR Evolution) using a 455 mW, 532 nm Nd:YAG laser (Laser Quantum), a non-dispersive filter to reduce the power at the sample to between ~50 and 100% of the laser power, a 600 g $mm^{-1}$ grating and a 20× objective (Olympus LMPLFLN20X). Each Raman spectrum was obtained as 10–15 accumulations of 10–15 s acquisitions.

## 3. Results and discussion

### 3.1 $CO_2$ flux with an alternating wet and dry sweep gas

A hydroxide-infiltrated membrane was heated to 600 °C with ~1% $H_2O$ in Ar supplied to both the feed- and permeate-side chamber inlets, before the feed-side chamber inlet was switched to 50% $CO_2$ in $N_2$ (the permeate-side chamber inlet remained as ~1% $H_2O$ in Ar). $CO_2$ flux was measured, before cycling between a dry (Ar with ≤3 ppm $H_2O$) and wet (~1% $H_2O$ in Ar) sweep gas (Fig. 3). Despite there being a $CO_2$ partial pressure difference across the membrane (*i.e.*, a $CO_2$ driving force), initially there was no significant $CO_2$ flux. At ~2.5 h, $CO_2$ flux 'breakthrough' occurred, before the $CO_2$ flux reached ~2.5 × $10^{-4}$ mol $s^{-1}$ $m^{-2}$. Upon switching to the dry sweep gas at 3 h, there was a decrease in $CO_2$ flux, reaching ~1 × $10^{-5}$ mol $s^{-1}$ $m^{-2}$ at 6 h. Note that hereafter, we frequently refer to fluxes on the order of $10^{-4}$ mol $s^{-1}$ $m^{-2}$ as 'high', and fluxes on the order of $10^{-5}$ mol $s^{-1}$ $m^{-2}$ as 'low', for simplicity, and due to the order-of-magnitude difference.

Further cycling between the wet and dry sweep gas resulted in a similar response from the membrane, *i.e.*, abrupt, order-of-magnitude changes between high and low $CO_2$ flux, and a clear

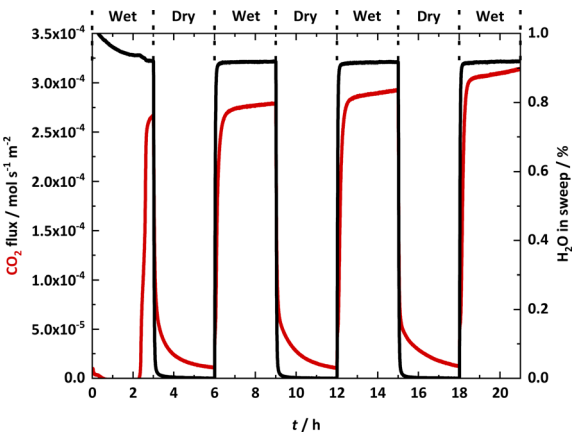


Fig. 3 $CO_2$ flux with an alternating wet and dry sweep gas. Feed-side chamber inlet: 50% $CO_2$ in $N_2$. Permeate-side chamber inlet: dry (Ar with ≤3 ppm $H_2O$) and wet (~1% $H_2O$ in Ar). $T$ = 600 °C.

link between the presence of $H_2O$ in the sweep gas and high $CO_2$ flux. It was also notable that the $CO_2$ flux in the wet cycles increased across the cycles. First, the high flux achieved at the end of the previous wet cycle was recovered quickly before the flux continued to increase slowly. As the conditions (temperature, $CO_2$ concentration in the feed gas, $H_2O$ concentration in the sweep gas *etc.*) of the wet cycles remained constant, this implied that the membrane composition might be changing in time. We note here that characterisation of the membrane support (SEM-EDX and Raman as described in Section 2.4) showed that even after ~800 h (>1 month) of membrane operation, there were no significant changes to the physical properties of the membrane support (Fig. S4†), and that there were only minor changes to the support chemistry (*e.g.*, limited formation of $LiAlO_2$) (Table S3 and Fig. S5†). This suggested that the order-of-magnitude changes in $CO_2$ flux occurring on much shorter timescales (between wet and dry cycles of 3 h) were more likely arising due to the presence of $H_2O$ in the sweep gas, and that changes occurring on even shorter timescales (breakthrough and increasing flux within wet cycles) may be due to an evolving molten-salt composition.

### 3.2 $CO_2$ flux as a function of time and $H_2O$ concentration in the feed and sweep gases

Considering the potential for changes in the molten salt with time, and a clear link between $CO_2$ flux and the presence of $H_2O$ in the sweep gas (Fig. 3), two series of experiments were conducted. In the first series, $CO_2$ flux and molten-salt composition (titrations with the recovered salt as described in Section 2.4), were measured as a function of time with fixed feed- and sweep-gas compositions (Fig. 4a). In the second series, the $H_2O$ concentration in the feed and sweep gas was varied, with the $CO_2$ flux and membrane composition measured after a fixed amount of time (Fig. 4b). All experiments were conducted at 600 °C. Thus, the first series investigated the effect of time in the presence of a $H_2O$-containing sweep gas, and the second series investigated the effect of $H_2O$ concentration in the $H_2O$-containing sweep gas (and in one case, the feed gas). To attempt to avoid any influence of membrane 'history', all experiments were carried out separately, *i.e.*, following recovery of the salt from the membrane support by washing (as described in Section 2.4), the membrane support was re-infiltrated with fresh molten hydroxides and tested at a different condition (recalling that no significant changes were noted in the membrane support following >1 month of operation). Examples of the full experimental traces (*i.e.*, mole fractions of $CO_2$, $N_2$ and $H_2O$ on the permeate side) from the permeation experiments and titration data are provided in Fig. S6 and Table S4† for the first series (Fig. 4a), and in Fig. S7 and Table S5† for the second series (Fig. 4b).

In the first series (effect of time), hydroxide-infiltrated membranes were heated to 600 °C with ~1% $H_2O$ in Ar supplied to both the feed- and permeate-side chamber inlets, before the feed-side chamber inlet was switched to 50% $CO_2$ in $N_2$ and the permeate-side chamber inlet was switched to ~0.5% $H_2O$ in Ar. After 0, 5, 10, 20, 30, 40, and 50 h of operation following the gas switches (in separate experiments), $CO_2$ flux was recorded (points in Fig. 4a) and triplicate titrations were carried out to characterise the recovered molten salt (bars in Fig. 4a).

First, it was noted again that there was a breakthrough period in all the experiments, after which $CO_2$ flux increased significantly in the absence of any other changes (Fig. S6†). The breakthrough period was of approximately the same duration in

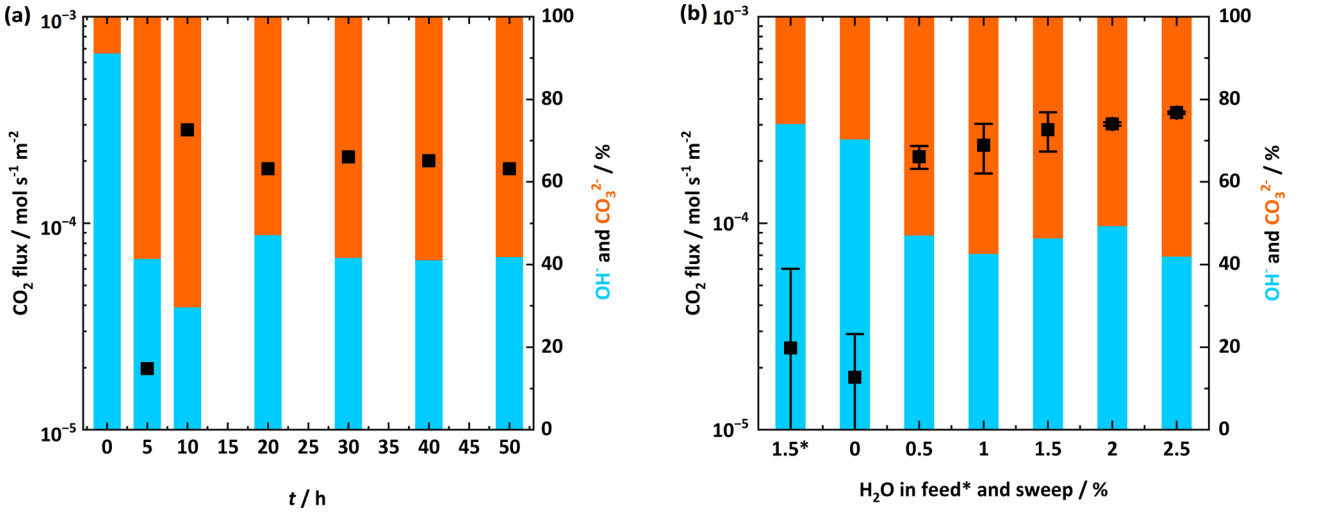


Fig. 4 $CO_2$ flux as a function of time and $H_2O$ concentration in feed and sweep gases. In both (a) and (b) points are $CO_2$ flux, and coloured bars are triplicate titrations of recovered salts. (a) $CO_2$ flux and titrations of recovered salts after separate experiments lasting for 0, 5, 10, 20, 30, 40, and 50 h. Feed-side chamber inlet: 50% $CO_2$ in $N_2$. Permeate-side chamber inlet: ~0.5% $H_2O$ in Ar. $T = 600$ °C. (b) Mean $CO_2$ flux with standard deviation ($n = 2$–4) and titrations of recovered salts after separate 20 h experiments with different $H_2O$ concentrations in feed (marked with an *) and sweep gas. Feed-side chamber inlet: 50% $CO_2$ in $N_2$ (with 1.5% $H_2O$ for *). Permeate-side chamber inlet: dry (Ar with ≤3 ppm $H_2O$) for * and 0, and ~0.5, 1, 1.5, 2, and 2.5% $H_2O$ in Ar. $T = 600$ °C. Full experimental traces and data for (a) are provided in Fig. S6, and Table S4†. Example experimental traces for (b) are provided in Fig. S7,† and the repeats used to calculate mean and error bars in (b) are provided in Table S5†.

 

each separate experiment (~5 h). For this reason, the $CO_2$ flux reported at 5 h in Fig. 4a is low as it is taken from transient data where $CO_2$ breakthrough is beginning (Fig. S6a†). Nonetheless, this makes for an interesting comparison, as it is notable that after 5 h, the molten-salt composition was relatively stable at ~60% carbonate : ~40% hydroxide (bars), whilst the $CO_2$ flux (points) was also high (on the order of $10^{-4}$ mol $s^{-1}$ $m^{-2}$). Although there are small differences in the $CO_2$ flux and composition, we must recall here that these results are taken from separate permeation experiments and their corresponding triplicate titrations, and that we are discussing an order-of-magnitude difference in $CO_2$ flux before and after breakthrough. We also note here that the 0 h membrane (heated to 600 °C with ~1% $H_2O$ in Ar supplied to both the feed- and permeate-side chamber inlets but cooled in dry Ar without being exposed to the 50% $CO_2$ in $N_2$ feed gas) had a recovered salt composition of ~10% carbonate : ~90% hydroxide. This is expected, as despite handling and preparing the hydroxide mixture under an inert gas in a glove box, atmospheric $CO_2$ will react with the hydroxide pellet during the amount of time required to prepare the membrane (between the hydroxides leaving the glove box and the permeation experiment starting), and during the time required to recover the hydroxides from the membrane afterwards (between the membrane being removed from the reactor and the titration being performed).

In the second series (effect of $H_2O$ concentration), hydroxide-infiltrated membranes were heated to 600 °C with ~1% $H_2O$ in Ar supplied to both the feed- and permeate-side chamber inlets, before the feed-side chamber inlet was switched to 50% $CO_2$ in $N_2$, as above. However, here the permeate-side chamber inlet was switched to ~0 (dry, Ar with ≤3 ppm $H_2O$), 0.5, 1.0, 1.5, 2.0, and 2.5% $H_2O$ in Ar in separate experiments. Additionally, in a further separate experiment, ~1.5% $H_2O$ was added to the 50% $CO_2$ in $N_2$ feed gas (with the sweep gas being dry Ar). As discussed in more detail below, the permeation experiments were repeated several times to assess experimental uncertainty (Table S5†). Following ~20 h at each condition, $CO_2$ flux was recorded (points in Fig. 4b are the mean and error bars are standard deviation from the repeated permeation experiments), and corresponding triplicate titrations were carried out (bars in Fig. 4b), before the membrane was reinfiltrated and tested at the next condition. Before discussing the results, we note again that there was a breakthrough period in every experiment of ~5 h, and that 20 h was chosen based on the results in Fig. 4a (*i.e.*, no significant change in molten-salt composition or $CO_2$ flux was expected).

First, it was apparent that under a dry sweep gas (Ar with ≤3 ppm $H_2O$), $CO_2$ flux was low and on the same order of magnitude ($10^{-5}$ mol $s^{-1}$ $m^{-2}$) as in the dry cycles of Fig. 3. Second, whilst adding ~1.5% $H_2O$ to the feed gas did not result in any significant increase in $CO_2$ flux, there was also no deleterious effect on $CO_2$ flux. This is important, as there are significant costs associated with drying feed gases to combat deleterious effects in other classes of membranes, *e.g.*, polymeric membranes.[6] When ~0.5% $H_2O$ was added to the sweep gas, however, the $CO_2$ flux increased, again by an order of magnitude to $10^{-4}$ mol $s^{-1}$ $m^{-2}$. Moreover, the $CO_2$ flux appeared to increase further as the $H_2O$ concentration in the sweep gas increased (Fig. 4b).

Considering that all the discussion so far has related to order-of-magnitude arguments, here we assessed experimental uncertainty by repeating $CO_2$ flux measurements for each condition up to four times (Table S5†). This repetition was to check whether any differences in $CO_2$ flux were beyond experimental uncertainty. Indeed, the $CO_2$ flux did increase with increasing $H_2O$ concentration in the sweep gas. Interestingly, the molten-salt composition showed a corresponding trend (bars in Fig. 4b). Under dry sweep-gas conditions and with $H_2O$ in the feed gas (when $CO_2$ flux was low, on the order of $10^{-5}$ mol $s^{-1}$ $m^{-2}$), the recovered salts were ~25% carbonate : ~75% hydroxide. Conversely, under wet sweep-gas conditions (when $CO_2$ flux was high, on the order of $10^{-4}$ mol $s^{-1}$ $m^{-2}$), the recovered salts were ~60% carbonate : ~40% hydroxide. We note that this composition is the same as that following breakthrough (at and after 5 h) in Fig. 4a.

Here it is important to highlight that the $CO_2$ flux in Fig. 4b is increasing as the $H_2O$ driving force in the opposite direction is increasing, as in our recent work with a molten-salt membrane fabricated using molten carbonates we showed that $CO_2$ flux can depend on the $H_2O$ driving force in the opposite direction (eqn (3)).[33] Considering the results in Fig. 4b, it seemed reasonable to suspect that the $H_2O$ driving force may be influencing $CO_2$ flux here also, but this time in a membrane fabricated using molten hydroxides. To test this hypothesis, the measurement of both permeate-side and feed-side outlet composition is required to see if $CO_2$ and $H_2O$ are counter-permeating, and to test the extent of the influence that the $H_2O$ driving force (from $CO_2$ permeate-side to $CO_2$ feed-side) has over $CO_2$ flux (from $CO_2$ feed-side to $CO_2$ permeate-side).

### 3.3 Measuring the counter-permeation of $CO_2$ and $H_2O$ and evidencing the role of the $H_2O$ driving force on $CO_2$ flux

To investigate the counter-permeation of $CO_2$ and $H_2O$, a hydroxide-infiltrated membrane was heated to 600 °C with ~1% $H_2O$ in Ar supplied to both the feed- and permeate-side chamber inlets, before the feed-side chamber inlet was switched to 50% $CO_2$ in $N_2$ and the permeate-side chamber inlet was switched to ~0 (dry, Ar with ≤3 ppm $H_2O$), 1, and 1.5% $H_2O$ in Ar, in a single, continuous experiment (Fig. 5). The $CO_2$ flux was calculated from the permeate-side outlet composition, and the $H_2O$ flux was calculated from the feed-side outlet composition. There was clear evidence for the counter-permeation of $H_2O$ and $CO_2$, *i.e.*, with increases in the concentration of $H_2O$ in the sweep gas, the fluxes of $H_2O$ and $CO_2$ (in opposite directions) both increased. Moreover, it appeared that the magnitude of the $CO_2$ and $H_2O$ fluxes were similar, suggesting that their permeation was linked (we note that this was also the case in our prior work with a membrane fabricated using molten carbonates).[33]

With the understanding that $CO_2$ and $H_2O$ counter-permeate, and that their permeation may be linked, it is therefore important to consider the role of the $H_2O$ driving force on $CO_2$ flux. Thus, in a final series of permeation experiments, the $CO_2$ driving

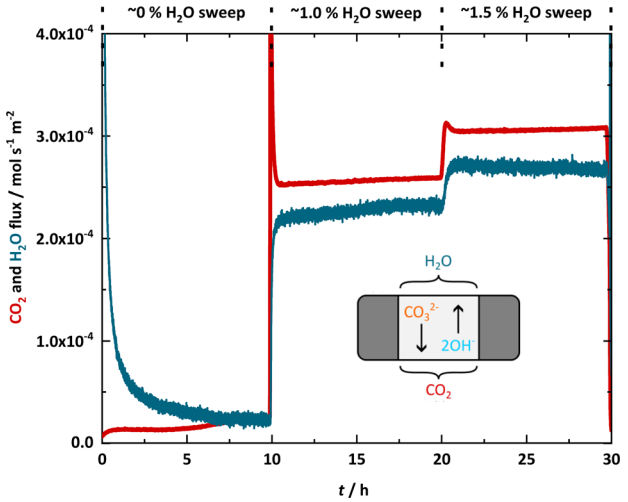


Fig. 5 Counter-permeation of $CO_2$ and $H_2O$. $CO_2$ flux (measured at the permeate-side outlet) and $H_2O$ flux (measured at the feed-side outlet), *i.e.*, in opposite directions (inset schematic). Feed-side chamber inlet: 50% $CO_2$ in $N_2$. Permeate-side chamber inlet: ~0 (dry Ar with ≤3 ppm $H_2O$), 1, and 1.5% $H_2O$ in Ar. $T$ = 600 °C.

force was increased whilst the $H_2O$ driving force in the opposite direction was held constant, and conversely, the $CO_2$ driving force was held constant whilst the $H_2O$ driving force in the opposite direction was increased. This was achieved by heating hydroxide-infiltrated membranes to 600 °C with ~1% $H_2O$ in Ar supplied to both the feed- and permeate-side chamber inlets, before the feed-gas chamber inlet was switched to 1.5, 10 or 50% $CO_2$ in $N_2$, whilst the permeate-side chamber inlet was switched to ~1, 1.5, or 2.0% $H_2O$ in Ar (Fig. 6). The results shown in Fig. 6 are from three separate experiments using the three different

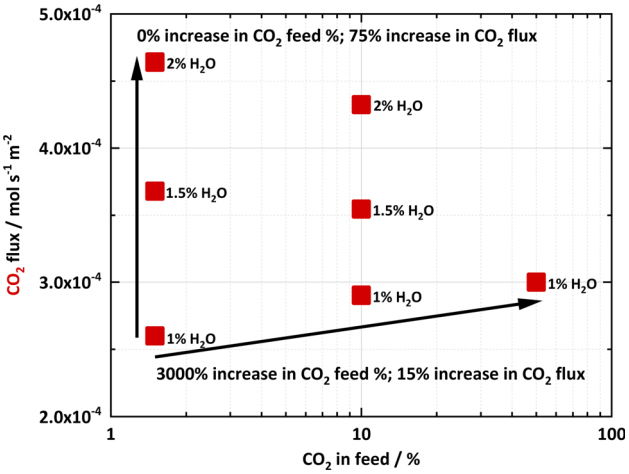


Fig. 6 The role of the $H_2O$ driving force on $CO_2$ flux. $CO_2$ flux measured at the permeate-side outlet. Feed-side chamber inlet: 1.5, 10, or 50% $CO_2$ in $N_2$. Permeate-side chamber inlet: ~1, 1.5, or 2.0% $H_2O$ in Ar. $T$ = 600 °C. Arrows highlight ~3000% increase in linear $CO_2$ driving force and corresponding ~15% increase in $CO_2$ flux, and 0% increase in linear $CO_2$ driving force and corresponding ~75% increase in $CO_2$ flux.

feed gases (1.5, 10, and 50% $CO_2$ in $N_2$). During the experiments with the 1.5 and 10% $CO_2$ in $N_2$ feed gases, the permeate-side chamber inlet was increased from ~1, to 1.5 and 2.0% $H_2O$ in Ar after 10 h at each condition. The $CO_2$ flux (points) is an average of 5 h of stable $CO_2$ flux, 5 h after the change in the permeate-side chamber inlet condition. During this 5 h period, the $CO_2$ flux was measured every 5 s, and the maximum variation in $CO_2$ flux was 6%.

With a ~3000% increase in feed-gas $CO_2$ concentration (from 1.5 to 50%), $CO_2$ flux increased by ~15% (which based on the results in Fig. 4b is within our experimental uncertainty). Whilst initially the lack of a significant increase in $CO_2$ flux with a significant increase in the $CO_2$ driving force might be surprising, this is due to the assumption that $CO_2$ flux should be linked only to the $CO_2$ driving force. If instead the $H_2O$ driving force is exerting control over the $CO_2$ flux, this result can be explained based on the ~1% $H_2O$ supplied for both feed-gas conditions, *i.e.*, the $CO_2$ driving force may not have a strong influence in the presence of $H_2O$ in the sweep gas.

We note that these results in Fig. 6 are consistent with the only previous article that studied a membrane fabricated using molten hydroxides.[32] In that work, the authors reported an unusual apparent $CO_2$ permeability increase as the feed-gas $CO_2$ concentration was decreased from 50 to 20% $CO_2$, whilst the sweep gas contained 4.5% $H_2O$. Based on their method to determine permeability (which assumed eqn (2) with $n = 1$), were the fluxes with the 50 and 20% $CO_2$ feed gases similar, the apparent permeability would be expected to increase by a factor of ~2.5 (*i.e.*, 50/20), which was indeed the case (from ~6.5 to ~16 × $10^{-11}$ mol $m^{-1}$ $Pa^{-1}$ $s^{-1}$).[32] Were we to use the same approach here, we would report a ~30-fold increase in apparent permeability (*i.e.*, 50/1.5), for $CO_2$ fluxes that are within our experimental uncertainty. Moreover, the authors suggested that the apparent increase in $CO_2$ permeability with a decrease in $CO_2$ driving force was likely due to the lower feed-gas $CO_2$ concentration resulting in a lowering of the carbonate : hydroxide ratio in the membrane during operation.[32] They suggested this as molten hydroxides have a higher ionic conductivity than molten carbonates, however, no direct experimental evidence was provided to support this assertion. Contrasting with this prior suggestion, our results from triplicate titrations carried out following further, separate experiments with 10 and 50% $CO_2$ feed gases, suggested that there was no significant difference in the carbonate : hydroxide ratio (Table S6†). It is also worth noting that these titrations were performed on salts recovered from permeation experiments with 10 and 50% $CO_2$ feed gases (and a ~1% $H_2O$ in Ar sweep gas) where the temperature was increased from 500, to 600, and 700 °C. The $CO_2$ fluxes at 700 °C for both feed gas conditions were the same at ~7 × $10^{-4}$ mol $s^{-1}$ $m^{-2}$, the highest reported in our work (Fig. S8†). Interestingly, the carbonate : hydroxide ratio was also the highest reported at ~80% carbonate : ~20% hydroxide (Table S6†). We also wish to highlight here again the results in Fig. 4b, where $CO_2$ flux increased with an increasing concentration of $H_2O$ in the sweep gas, but the composition of the membrane remained relatively constant at ~60% carbonate : ~40% hydroxide. Thus, overall, it seems likely that

 

a lowering of the carbonate : hydroxide ratio may not explain increases in $CO_2$ flux, as across several of our experiments, high $CO_2$ fluxes are correlated with high carbonate : hydroxide ratios. Moreover, although $CO_2$ permeability can be made to increase with a reduction in the $CO_2$ feed-gas concentration, this is simply due to the use of a linear $CO_2$ driving force (assuming eqn (2) with $n = 1$) in the calculation of $CO_2$ permeability when the $CO_2$ flux is not changing significantly (due to the influence of the opposing $H_2O$ driving force).

Finally, and to demonstrate very clearly the importance of controlling the opposing $H_2O$ driving force, the $H_2O$ concentration in the sweep gas was increased whilst the feed-gas chamber inlet was held constant at 1.5 or 10% $CO_2$ in $N_2$. Despite 1.5% $CO_2$ being the lowest feed-gas $CO_2$ concentration employed in our work (and therefore the lowest $CO_2$ driving force), the $CO_2$ flux was at the highest level we report at 600 °C (>$4.5 \times 10^{-4}$ mol $s^{-1}$ $m^{-2}$). This was achieved by increasing the $H_2O$ concentration in the sweep gas from ~1, to 1.5, and 2% (Fig. 6), which increased the opposing $H_2O$ driving force (Fig. 1d). This ~100% increase in the opposing $H_2O$ driving force had a much more significant effect on $CO_2$ flux (~75% increase) than that of a ~3000% increase in $CO_2$ driving force, which resulted in a ~15% increase in $CO_2$ flux. Moreover, the ~75% increase in $CO_2$ flux is occurring without an increase in $CO_2$ driving force. Thus, whereas one might expect the $CO_2$ driving force, not the opposing $H_2O$ driving force, to exert more significant control on $CO_2$ flux, it appears that both the $CO_2$ and $H_2O$ driving forces impact $CO_2$ flux, but that the opposing $H_2O$ driving force has a much more significant effect (compare arrows in Fig. 6).

We note here that our discussion of *e.g.*, a ~100% increase in the opposing $H_2O$ driving force, and a ~3000% increase in $CO_2$ driving force (both also labelled on Fig. 6) is based on assuming linear driving force models (for simplicity of discussion). However, it is also apparent that none of the previously proposed $CO_2$ flux-driving force relationships (eqn (1)–(3)), including the linear model (eqn (2) with $n = 1$), can describe the results in Fig. 6 adequately, and that a much more complex relationship exists between the measured $CO_2$ flux and the partial pressures of the gases present. To develop such relationships, considering the four partial pressures involved ($CO_2$ on the feed and permeate side, and $H_2O$ on the feed and permeate side), we note that this becomes a very large, multi-dimensional kinetic space to sample.

## 4. Conclusions

Detailed understanding of promising $CO_2$-permeable membranes is important for the future CCS sector. In this work, we have carefully interrogated a model molten-salt membrane to understand the role of $H_2O$ on $CO_2$ flux. Whilst it had been shown previously that $CO_2$ flux increases when $H_2O$ is introduced to the sweep gas of molten-salt membranes fabricated using molten carbonates and molten hydroxides, prior attempts at explaining this phenomenon invoked arguments based on a higher ionic conductivity of molten hydroxides compared to molten carbonates. Instead, in this work, we have shown that a molten-salt membrane fabricated using molten hydroxides becomes majority molten carbonate (~60%) following breakthrough of $CO_2$, which then remains majority molten carbonate under conditions that provide high $CO_2$ fluxes (*i.e.*, with $H_2O$ in the sweep gas). Conversely, the membrane remains majority molten hydroxide (~75%) under conditions that provide low $CO_2$ fluxes (under a dry sweep gas and when $H_2O$ is present only in the feed gas). Increasing the $H_2O$ concentration in the sweep gas did not appear to modify the molten-salt composition further, but the $CO_2$ flux did increase further. Thus, both molten-salt composition and $H_2O$ driving force exert control over $CO_2$ flux in molten-salt membranes fabricated using molten hydroxides.

To demonstrate the importance of the $H_2O$ driving force, several examples were provided where the careful application of the $H_2O$ driving force (in the opposite direction to the $CO_2$ driving force and $CO_2$ flux) was used to challenge our routine understanding of $CO_2$-permeable membranes. This included driving $CO_2$ flux from 1.5 and 10% $CO_2$ feed gases to levels higher than that achieved with a 50% $CO_2$ feed gas. Interestingly, the highest $CO_2$ fluxes (~$7 \times 10^{-4}$ mol $s^{-1}$ $m^{-2}$ at 700 °C for both the 10 and 50% $CO_2$ feed gases with a ~1% $H_2O$ in Ar sweep gas) were correlated with the highest carbonate content in the molten salt (~80%).

Overall, our results suggest that the composition of the molten salt in a molten-salt membrane is a function of time, temperature, and gas-phase composition, which is why we have been careful throughout to refer to different molten-salt membranes as being fabricated using a given molten salt. Moreover, controlling the $H_2O$ driving force in the opposite direction to $CO_2$ permeation is required to exploit the potential of molten-salt membranes, and calculations intended to communicate this performance clearly (*e.g.*, $CO_2$ permeability) must be considered in this context. For example, calculating a $CO_2$ permeability using a linear $CO_2$ driving force may be somewhat meaningless when there is an opposing $H_2O$ driving force, as one can arrive at very different apparent $CO_2$ permeabilities when the $CO_2$ flux has not changed (and *vice versa*). For this reason, as is common practice with *e.g.*, temperature and $CO_2$ feed-gas concentration, measuring and reporting the sweep-gas $H_2O$ concentration alongside $CO_2$ permeability should now be required.

## Data availability

The data presented in this work is available at **https://data.ncl.ac.uk/**, DOI: **https://doi.org/10.25405/data.ncl.26335333**.

## Author contributions

JAP (investigation); JAP and WH (formal analysis, validation); JAP and GAM (visualization, writing – original draft, data curation); JAP, ISM and GAM (conceptualization, methodology); JAP, WH, ISM and GAM (writing – review & editing); ISM and GAM (supervision, project administration, funding acquisition, resources).

## Conflicts of interest

There are no conflicts to declare.

## Acknowledgements

This work was supported by the Engineering & Physical Sciences Research Council [grant numbers EP/V047078/1, EP/W03395X/1, EP/Y034961/1]. ISM acknowledges funding from the Royal Academy of Engineering through a Chair in Emerging Technologies Award entitled "Engineering Chemical Reactor Technologies for a Low-Carbon Energy Future" (Grant CiET1819/2/57). GAM was supported by the Royal Academy of Engineering under the Research Fellowship scheme. The authors are grateful to Dr Ingham of IGIsystems for helpful discussions during the design and operation of the flow system, and to the Electron Microscopy and Analysis Unit, SAgE Analytical, Newcastle University for assistance with the SEM-EDX measurements.

## Notes and references

1 M. Bui, C. S. Adjiman, A. Bardow, E. J. Anthony, A. Boston, S. Brown, P. S. Fennell, S. Fuss, A. Galindo, L. A. Hackett, H. J. Herzog, G. Jackson, J. Kemper, S. Krevor, G. C. Maitland, M. Matuszewski, I. S. Metcalfe, C. Petit, G. Puxty, J. Reimer, D. M. Reiner, E. S. Rubin, S. A. Scott, N. Shah, B. Smit, J. P. M. Trusler, P. Webley, J. Wilcox and N. MacDowell, *Energy Environ. Sci.*, 2018, **11**, 1062–1176.

2 D. Danaci, M. Bui, C. Petit and N. Mac Dowell, *Environ. Sci. Technol.*, 2021, **55**, 10619–10632.

3 M. Erans, E. S. Sanz-Pérez, D. P. Hanak, Z. Clulow, D. M. Reiner and G. A. Mutch, *Energy Environ. Sci.*, 2022, **15**, 1360–1405.

4 M. Fajardy and N. Mac Dowell, *Energy Environ. Sci.*, 2017, **10**, 1389–1426.

5 R. W. Baker, B. Freeman, J. Kniep, Y. I. Huang and T. C. Merkel, *Ind. Eng. Chem. Res.*, 2018, **57**, 15963–15970.

6 S. E. Zanco, J.-F. Pérez-Calvo, A. Gasós, B. Cordiano, V. Becattini and M. Mazzotti, *ACS Eng. Au*, 2021, **1**, 50–72.

7 R. Hou, C. Fong, B. D. Freeman, M. R. Hill and Z. Xie, *Sep. Purif. Technol.*, 2022, **300**, 121863.

8 G. A. Mutch, L. Qu, G. Triantafyllou, W. Xing, M. L. Fontaine and I. S. Metcalfe, *J. Mater. Chem. A*, 2019, **7**, 12951–12973.

9 B. Comesana-Gandara, J. Chen, C. G. Bezzu, M. Carta, I. Rose, M.-C. Ferrari, E. Esposito, A. Fuoco, N. B. McKeown and J. C. Jansen, *Energy Environ. Sci.*, 2019, **12**, 2733–2740.

10 T. C. Merkel, H. Lin, X. Wei and R. Baker, *J. Membr. Sci.*, 2010, **359**, 126–139.

11 J. L. Wade, C. Lee, A. C. West and K. S. Lackner, *J. Membr. Sci.*, 2011, **369**, 20–29.

12 M. Kazakli, G. A. Mutch, L. Qu, G. Triantafyllou and I. S. Metcalfe, *J. Membr. Sci.*, 2020, **600**, 117855.

13 M. Kazakli, G. A. Mutch, G. Triantafyllou, A. G. Gil, T. Li, B. Wang, J. J. Bailey, D. J. L. Brett, P. R. Shearing, K. Li and I. Metcalfe, *J. Membr. Sci.*, 2021, **617**, 118640.

14 W. Xing, T. Peters, M. L. Fontaine, A. Evans, P. P. Henriksen, T. Norby and R. Bredesen, *J. Membr. Sci.*, 2015, **482**, 115–119.

15 M. Anderson and Y. S. Lin, *J. Membr. Sci.*, 2010, **357**, 122–129.

16 E. I. Papaioannou, H. Qi and I. S. Metcalfe, *J. Membr. Sci.*, 2015, **485**, 87–93.

17 N. Xu, X. Li, M. A. Franks, H. Zhao and K. Huang, *J. Membr. Sci.*, 2012, **401–402**, 190–194.

18 J. Fang, N. Xu, T. Yang, P. Zhang, J. Tong and K. Huang, *J. Membr. Sci.*, 2017, **523**, 439–445.

19 L. A. McNeil, G. A. Mutch, F. Iacoviello, J. J. Bailey, G. Triantafyllou, D. Neagu, T. S. Miller, E. I. Papaioannou, W. Hu, D. J. L. Brett, P. R. Shearing and I. S. Metcalfe, *Energy Environ. Sci.*, 2020, **13**, 1766–1775.

20 Z. Xu, Q. Zheng, S. Wang, Z. Zhang, Z. Liu, G. Zhang and W. Jin, *J. Membr. Sci.*, 2021, **635**, 119506.

21 X. Dong, J. Ortiz Landeros and Y. S. Lin, *Chem. Commun.*, 2013, **49**, 9654–9656.

22 X. Dong, H.-C. Wu and Y. S. Lin, *J. Membr. Sci.*, 2018, **564**, 73–81.

23 S. Tsochataridou, G. A. Mutch, D. Neagu, E. I. Papaioannou, M. L. Sanjuán, B. Ray, R. I. Merino, V. M. Orera and I. S. Metcalfe, *ACS Appl. Mater. Interfaces*, 2020, **12**, 16436–16441.

24 Z. Rui, M. Anderson, Y. S. Lin and Y. Li, *J. Membr. Sci.*, 2009, **345**, 110–118.

25 J. Ortiz-Landeros, T. Norton and Y. S. Lin, *Chem. Eng. Sci.*, 2013, **104**, 891–898.

26 J. Y. S. Lin and O. Ovalle-Encinia, *J. Membr. Sci. Lett.*, 2023, **3**, 100041.

27 S. G. M. Carvalho, E. N. S. Muccillo, F. C. Fonseca, M. Müller, F. Schulze-Küppers, S. Baumann, W. A. Meulenberg, O. Guillon and R. Muccillo, *J. Membr. Sci.*, 2022, **648**, 120355.

28 L. Grima, G. A. Mutch, P. B. Oliete, W. Bucheli, R. I. Merino, E. I. Papaioannou, J. J. Bailey, M. D. Kok, D. J. L. Brett, P. R. Shearing, I. S. Metcalfe and M. L. Sanjuán, *J. Membr. Sci.*, 2021, **630**, 119057.

29 F. M. B. Marques, S. G. Patrício, E. Muccillo and R. Muccillo, *Electrochim. Acta*, 2016, **210**, 87–95.

30 K. Zhang, S. Sun, N. Xu and K. Huang, *J. Membr. Sci.*, 2022, **650**, 120421.

31 S. Sun, Y. Wen and K. Huang, *ACS Sustainable Chem. Eng.*, 2021, **9**, 5454–5460.

32 M. R. Cerón, L. S. Lai, A. Amiri, M. Monte, S. Katta, J. C. Kelly, M. A. Worsley, M. D. Merrill, S. Kim and P. G. Campbell, *J. Membr. Sci.*, 2018, **567**, 191–198.

33 I. S. Metcalfe, G. A. Mutch, E. I. Papaioannou, S. Tsochataridou, D. Neagu, D. J. L. Brett, F. Iacoviello, T. S. Miller, P. R. Shearing and P. A. Hunt, *Nat. Energy*, 2024, **9**, 1074–1083.

34 T. Terai, H. Mohri and Y. Takahashi, *J. Nucl. Mater.*, 1991, **179–181**, 808–811.

35 E. P. Partridge and W. C. Schroeder, *Ind. Eng. Chem., Anal. Ed.*, 1932, **4**, 271–273.

36 A. A. Benedetti-Pichler, M. Cefola and B. Waldman, *Ind. Eng. Chem., Anal. Ed.*, 1939, **11**, 327–332.

 